A Computational Analysis of Boundary Layer Instability over the BOLT Configuration

Meelan Choudhari* and Fei Li†
NASA Langley Research Center, Hampton, VA, 23681

Pedro Paredes‡
National Institute of Aerospace, Hampton, VA, 23666

The complex boundary layer flow over the BOLT flight configuration is known to exhibit multiple and potentially interacting instability mechanisms. This paper represents a continuation of our numerical investigation of the flow instabilities over the main test surface of the BOLT configuration by using state-of-the-art tools in multidimensional instability analysis. Specifically, the paper extends our previous computations by considering the separate effects of a nonzero angle of attack and a nonzero yaw on the modal instability characteristics of the boundary layer streaks adjacent to the minor-axis symmetry plane, specifically near both ends of the azimuthal region of a thick boundary layer in the middle, where this region rapidly changes to a thinner boundary layer on either side. At the t = 28.8767 s condition from the ascent part of the anticipated flight trajectory with a flight Mach number of M_∞ = 5.53 and unit Reynolds number of 4.25×10^6/m, either type of departure from the design condition is shown to have a considerable impact on the structure of the basic state rollup within the region of interest and, hence, also on the amplification characteristics of instability waves within the resulting streaks. Yet, for a yaw angle of β = 4 degrees, the computations indicate only a slight reduction with respect to the peak N-factor of nearly 11 at the design condition of zero degrees yaw and zero degrees angle of attack. In contrast, an angle of attack equal to α = 4 degrees, the peak N-factor decreases to nearly 6 on the leeward side and increases above 16 on the windward side, making the onset of transition highly likely on the windward side. Computations also highlight the role of streak instabilities that originate as Mack mode disturbances and also demonstrate the potential pitfalls in using surface pressure sensors alone to gauge the magnitude of instability amplification.

Nomenclature

c_{ph} = phase velocity along boundary layer edge streamline at the center plane [m/s]
f = frequency of instability waves [kHz]
h = specific enthalpy [J/kg]
L = axial body length equal to 0.866 m
M = Mach number (nondimensional)
M_∞ = freestream Mach number (nondimensional)
M_e = Mach number at the edge of the boundary layer (nondimensional)
N_E = N-factor based on disturbance (nondimensional)
N_{pw} = N-factor based on peak surface pressure fluctuation (nondimensional)
P_∞ = freestream pressure [Pa]
Pr = Prandtl number (nondimensional)
$\dot{q}$ = surface heat flux [W/m^2]
Re_L = Reynolds number based on body length (nondimensional)
Re_∞ = freestream unit Reynolds number [m^{-1}]
St = Stanton number (nondimensional) = $(\dot{q}/\rho_\infty U_\infty)/(h_{0,\infty} - h_{0,w})$
t = time [s]

---

* Aerospace Technologist, Meelan.M.Choudhari@nasa.gov, Fellow, AIAA.
† Aerospace Technologist, Fei.Li@nasa.gov
‡ Senior Research Engineer, pedro.paredes@nasa.gov, Senior Member, AIAA.

T_0 = stagnation temperature [K]
T_{ad} = adiabatic wall temperature [K]
T_w = wall temperature [K]
T_∞ = freestream temperature [K]
u = streamwise velocity [m/s]
u' = streamwise velocity fluctuation normalized to a peak value of unity at given location (nondimensional)
U_∞ = freestream velocity [m/s]
X = axial coordinate [m]
Y = coordinate along major axis of model cross section [m]
Z = coordinate along minor axis of model cross section [m]
α = angle of attack [deg]
β = yaw angle [deg]
σ = spatial growth rate [m^{-1}]
$\delta_{0.995}$ = boundary layer thickness based on $h_0/h_{0\infty} = 0.995$
ρ = fluid density [kg/m^3]

Subscripts
0 = stagnation condition
e = edge of the boundary layer based on $h_0/h_{0\infty} = 0.995$
w = wall
∞ = freestream

Abbreviations
BOLT = boundary layer transition
DNS = direct numerical simulations
HIFiRE = hypersonic international flight research experimentation
MM = Mack mode
PNP = partially nonparallel
PSE = parabolized stability equations
SI = streak instability
WENO = weighted essentially nonoscillatory

I. Introduction

Variability in the transition onset location can account for a major part of the overall uncertainty in the predicted heat loads on the surface of a hypersonic flight vehicle. Therefore, accurate estimates of laminar-turbulent boundary layer transition is an important aspect of the aerothermodynamic modeling of these vehicles. Wind tunnel experiments have played a crucial role in guiding the development of transition prediction models for low-speed flows. However, the transition process in conventional supersonic and hypersonic facilities tends to be dominated by the high levels of freestream disturbances associated with the acoustic radiation from the turbulent boundary layers along the wind tunnel walls. While low-disturbance facilities, i.e., the so-called quiet wind tunnels can better mimic the inflight transition process, the existing ground facilities of this type are often limited to subscale models. Thus, flight measurements of boundary layer transition are particularly important for the development of reliable models for boundary layer transition over high-speed vehicles.

Transition over high-speed vehicles is often dominated by the effects of unavoidable surface roughness. However, transition prediction for smooth surfaces provides a valuable reference to gauge the effects of the roughness. Earlier flight experiments involving canonical body shapes with nominally smooth surfaces provided transition data for circular cones at supersonic [1] and hypersonic flight speeds [2–4]. Other notable examples of high-speed transition experiments include the Pegasus flight experiment that provided crossflow transition measurements over a specially designed wing glove and the Hyper-X (X-43) flight data [5] that was likely dominated by Mack mode transition over the upper surface of the vehicle [6]. The subsequent flight experiments involving circular cone (HIFiRE-1) and elliptic cone (HIFiRE-5) configurations have provided more detailed measurements toward the calibration of stability-based models for the transition mechanisms related to the Mack mode and crossflow instabilities, respectively [7–10]. The HIFiRE-5b configuration also exhibited an additional, complex flow feature in the form of a centerline streak near the minor-axis symmetry plane that is likely to have transitioned via shear-layer instabilities that are concentrated within one or more localized regions of high shear within the streak [11−13]. Building upon the success of the HIFiRE-1 and HIFiRE-5b flight campaigns, the BOLT flight experiment [14] will focus on a more complex geometric configuration. The BOLT configuration (Fig. 1) shares certain geometric and flowfield features with the HIFiRE-5b elliptic cone but also exhibits a few key differences in the model geometry that result in a more complex basic state than HIFiRE-5b. For overviews of the BOLT flight campaign, the reader is referred to the papers by Wheaton et al. [14, 15].

The BOLT geometry includes a 2D nose tip with four swept leading edges curving around from the spanwise ends of the tip. These four leading edges are joined by four laterally concave surfaces, each of which has a single plane of symmetry. The top side of the BOLT configuration corresponds to the main test surface, denoted as side A, whereas the bottom surface (or side B that is also referred to as the "secondary" side) will be used to acquire additional measurements for the effects of a backward facing step. The strongly concave gutter regions on the lateral sides were designed to isolate the flows on sides A and B, respectively. As part of the preflight investigations, Berridge et al. [16] conducted experiments on subscale BOLT models in the Boeing/AFOSR Mach 6 Quiet Tunnel (BAM6QT) at Purdue University and a full scale model in the LENS II facility at CUBRC. The surface pressure measurements obtained during both of these tests revealed the presence of narrow band, high-frequency spectral peaks that were indicative of an instability mechanism of some type. However, the nature of these instabilities could not be determined. Additional measurements in both quiet and conventional wind tunnels at Texas A & M University [17, 18] also indicated the presence of a spectral hump in the surface pressure measurements near the center plane of the test surface, i.e., near the minor-axis plane of symmetry of the BOLT configuration. Additional measurements based on hot wire anemometry were used to provide extra information about the crossplane distribution of the velocity fluctuations within a limited part of the model cross section. Additional spectral peaks in other areas of the test surface were measured in the BAMQT by Berridge et al. [13], including a peak that was attributed to a travelling crossflow instability and another peak along the outboard edge of the thick vortical region near the center plane.

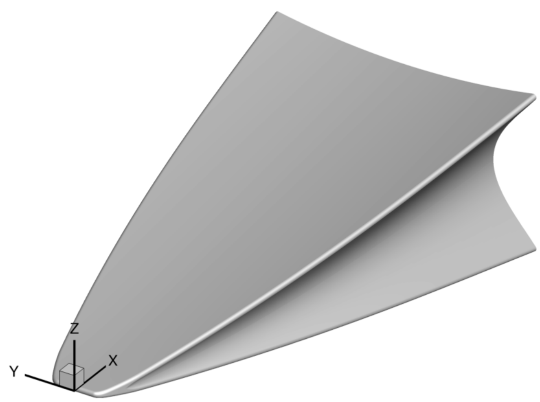

Figure 1. Schematic of the BOLT geometry. Side A corresponds to the top surface and Side B is the bottom surface that is hidden in this figure.

Thermographic measurements of a subscale BOLT configuration in the NASA Langley 20-Inch Mach 6 Air Tunnel by Berry et al. [20] revealed a prominent two-lobed transition pattern within the crossflow dominated region closer to the attachment lines along with transition along the center plane that was less obvious from the heat transfer imaging. The onset of transition was sensitive to the flow Reynolds number, but only weakly dependent on the angle of attack. On the other hand, a nonzero yaw resulted in a strongly asymmetric transition pattern on the test surface.

Direct numerical simulations (DNS) of the BOLT flight configuration at the University of Minnesota [21−23] revealed the presence of prominent, streamwise elongated vorticity structures along the test surface. The DNS methodology was extended to account for the effects of conjugate heat transfer in Ref. [24]. The thermal footprint of the computed vorticity structures was in good agreement with the measurements in the quiet flow experiments [21, 22]. The DNS also indicated the presence of four different types of nonstationary disturbances amplifying within the boundary layer flow, namely, those concentrated within the streaks along the outboard portions of the thickened boundary layer adjacent to the center plane, traveling crossflow disturbances inboard of the attachment line, a Mack mode instability that amplified in two different azimuthally localized regions, and the so-called mixed modes with a broad range of frequencies within the midspan region. Moyes et al. [25] analyzed the stability characteristics of the BOLT boundary layer and found significantly large N-factor values for the Mack mode instabilities in the region of adverse pressure gradient near the leading edge, as well as a strong amplification of crossflow instability modes within a wedge-shaped region on either side of the center plane. Even though some of the stationary streaks included in the DNS solutions from Refs. [22, 23] were not captured in the basic state computations with a second-order accurate, upwind-biased CFD scheme, Moyes at al. [26] showed that the streak evolution within the DNS solution could also be captured in the computations based on the nonlinear parabolized stability equations (PSE) by suitably tuning the initial disturbance amplitudes.

Berridge et al. [19] highlighted the lack of understanding of the transition mechanisms in the vicinity of the centerline as an important need. A recent analysis by Li et al. [27] showed that the streak instabilities adjacent to the BOLT center plane are analogous to those on the HIFiRE-5 elliptic cone, but that there are also important differences between the two because the streaks over the BOLT always remain at a finite distance from the center plane. There was encouraging agreement between the predicted frequency range of the streak instabilities and those measured in the experiments at TAMU. The computations also confirmed the strong effects of the flow Reynolds number on the amplification factors of streak instabilities, in agreement with the experimental observations by Berry et al. [20]. The investigation by Li et al. [27] also indicated the effects of a nonzero angle of attack and a nonzero yaw on the streak patterns within the boundary layer. However, no detailed analysis of either the basic state structures or the instabilities thereof was carried out. The present work denotes the continuation of that study to document the basic state and instability characteristics of the flow adjacent to the centerplane, including the N-factor curves for the relevant modes of instability within that region. A description of the flow configuration and the computational methodology is given in Section II. The laminar basic states at the flow conditions of interest are described in Section III, and the results of the instability analysis are presented in Section IV. Conclusions are presented in Section V.

II. Flow Configuration and Numerical Methodology

As mentioned in the Introduction, the flow configuration of interest corresponds to the BOLT configuration from Fig. 1. The flight article is 0.866 meters long, with a base width and base height of 0.438 meters and 0.256 meters, respectively. The BOLT geometry is symmetric about two mutually orthogonal planes and we denote the normal directions to these planes as the Y and Z axes of a Cartesian coordinate system, with the X axis along the axis of the model. The BOLT configuration differs from the HIFiRE-5 elliptic cone by virtue of its 2D nose tip with a twice as large nose radius (5 mm versus 2.5 mm for the HIFiRE-5 model) and a cross-section with concave transverse curvature on all four sides. However, the centerline geometry ($Y = 0$) of both configurations corresponds to a planar wedge inclined at 7 degrees with respect to the major-axis plane of symmetry (i.e., $Z = 0$).

As described by Li et al. [27], the basic state computations employ a two-step strategy, starting with a precursor computation based on the second-order, shock capturing code VULCAN (Viscous Upwind aLgorithm for Complex flow ANalysis) [28]. The VULCAN solution provides the boundary conditions for a higher-order DNS code focused on the flow downstream of the nose region and underneath the bow shock. All of the basic state computations assume the fluid to be a perfect gas (air) and the usual constitutive relations for a Newtonian fluid are used, namely, the viscous stress tensor is linearly related to the rate-of-strain tensor and the heat flux vector scales linearly with the temperature gradient through Fourier's law. The coefficient of viscosity is computed from Sutherlands's law and the coefficient of thermal conductivity is computed by assuming a constant Prandtl number (Pr = 0.72).

The VULCAN code solves the unsteady, conservation equations appropriate for a laminar or turbulent flow of calorically or thermally perfect gases with a spatially second-order accurate cell-centered finite volume scheme. A variety of upwind schemes are available for fine-tuning of numerical dissipation and shock capturing in order to ensure solution accuracy for stability computations. In the present computations, the inviscid fluxes were constructed using the MUSCL κ=0 scheme, the van Albada gradient limiter [29] and the Low Dissipation Flux Split Scheme (LDFSS) of Edwards [30]. The cell face gradients required to construct the viscous fluxes were obtained using an auxiliary control volume approach that results in a compact viscous stencil that produces a second-order accurate approximation of the full Navier-Stokes viscous fluxes. The solutions were relaxed in pseudotime to steady state by using the 3D ILU(0) scheme [31] with a constant CFL number of 20. Due care was taken to ensure that the grid was aligned with the shock surface so as to avoid the generation of spurious flow features, especially within the nose region.

The basic states used for instability analysis were obtained by using higher-order computations based on the DNS-WENO code that derive the inflow and freestream boundary conditions from the VULCAN solutions. A detailed description of the governing equations and the numerical algorithms used in the DNS-WENO code is given by Wu and Martin [32]. For brevity, this code is henceforth referred to as simply the DNS code. The inviscid fluxes from the governing equations are computed using a seventh-order weighted essentially nonoscillatory (WENO) finite-difference as introduced by Jiang and Shu [33], and the DNS-WENO code also includes an optimized scheme that reduces the numerical dissipation by means of limiters [34]. Both an absolute limiter on the WENO smoothness measurement and a relative limiter on the total variation are employed simultaneously during the simulation. The viscous fluxes are discretized by using a fourth-order central difference scheme and the time integration is based on a third-order low-storage Runge-Kutta scheme [35]. The DNS code has also been used in the study of centerline transition on the HIFiRE-5b model and the evolution of the streak instabilities based on the DNS was in excellent agreement with the predictions of the plane marching PSE [11].

The specific cases investigated thus far are outlined in Table 1, and the sizes of the computational grids used in each case are listed in Tables 2 and 3 for the VULCAN and the DNS computations, respectively. We use the same case designation as that of Li et al. [27], who used the identifier FAL (i.e., Flight-Ascent-Low Reynolds number) to denote the two cases of interest in this paper. The subscript 'b' in the mesh designation refers to the baseline mesh resolution. Exploiting the symmetry of the BOLT geometry, only the appropriate half of the model was used for each the two cases corresponding to a nonzero α and nonzero β, respectively. The lack of grid sensitivity of the basic state computation on the grids used herein was confirmed in Ref. [27] for the $\alpha = \beta = 0$ case.

Table 1 Flow configurations and associated freestream conditions.

Case Designation	*BOLT configuration*	α (deg)	β (deg)	M_∞	Re_∞ (m^{-1})	Re_L	U_∞ (m/s)	P_∞ (Pa)	T_∞ (K)	T_w (K)
FAL_α	Ascent (t = 28.8767 s)	4	0	5.53	4.25M	3.68M	1650.9	2380.2	222.0	400.00
FAL_β		0	4							

Table 2 Mesh parameters for VULCAN computations.

Case Number	*Mesh*	*Leading Edge Block*	*Main Part of BOLT Model*
FAL_α	V-$FAL_{2Z,b}$	289×257×301	1121×833×301
FAL_β	V-$FAL_{2Y,b}$	577×129×301	1121×833×301

Table 3 Mesh parameters for DNS-WENO computations.

Case Number	*Mesh*	*Leading Edge Block*	*Main Part of BOLT Model*
FAL_α	$FAL_{2Z,b}$	N/A	526×1238×246
FAL_β	$FAL_{2Y,b}$	N/A	526×1217×246

The stability of the basic states computed in this manner is investigated by using a combination of local, multidimensional eigenvalue analysis and plane-marching parabolized stability equation (PSE) implementation [36]. The analysis of instability modes within the boundary layer streaks must account for the enhanced azimuthal gradients associated with the streaks within the region of interest, which correspond to relatively compact azimuthal regions (relative to the overall width of the body) on either side of the inviscid streamline from the center of the nose tip (i.e., $X = Y = 0$). As seen later in Section III, this region corresponds to a narrow subset of the test surface in the vicinity of the center plane (i.e., $Y = 0$) for all cases with a zero yaw angle. For a nonzero yaw angle, the above region is inclined with respect to the $Y = 0$ plane at approximately the same angle as the yaw direction. For $\beta = 0$ degrees, the basic state is symmetric about the center plane, and hence, it is more convenient to restrict the stability analysis to the $Y > 0$ side, with the flow disturbances assumed to be either symmetric or antisymmetric with respect to the $Y = 0$ plane [11, 27]. The symmetric modes have zero azimuthal gradient in the axial velocity fluctuation component u' (as well as in the fluctuations in the surface normal velocity and all thermodynamic variables) at $Y = 0$, whereas the antisymmetric modes are associated with homogeneous Dirichlet boundary conditions in those quantities.

A typical grid size used for the eigenvalue computations and the plane marching PSE corresponds to 121 to 161 points in the wall-normal direction and between 201 to 401 points in the azimuthal direction. In a majority of the computations, the azimuthal domain is truncated a short distance beyond the region of strong streaks adjacent to the center plane.

III. Basic States

Computational results pertaining to basic state computations for the two flow configurations of interest are presented in this section. The surface distributions of the Stanton number for the FAL$_\alpha$, and FAL$_\beta$ are plotted in Figs. 2(a) and 2(b), respectively. Both the angle of attack and the yaw produce a clearly visible effect on the number of prominent thermal streaks, their locations, and strengths. Significant differences are seen between the streak patterns along the windward and leeward segments of the test surface in both Figs. 2(a) and 2(b). In particular, a prominent set of hot and cold streaks is observed in close proximity to the attachment line along the leeward surface for case FAL$_\alpha$. The FAL$_\beta$ case also shows a prominently asymmetric streak pattern over the test surface, with multiple strong roll-ups on the windward side. Prior to the completion of this work, the authors also became aware of the computations by Mullen and Reed [37], who examined the sensitivity of the stability characteristics to off-design conditions. Whereas the present work is focused on larger values of α and β that correspond to the maximum excursions targeted during the flight experiment and by the off-design condition explored in Refs. [16,19], the analysis in Ref. [37] was aimed at understanding the effects of smaller changes from the design condition. Furthermore, their work focused on the crossflow and second mode instability mechanisms in the outboard region of the test surface, whereas the present work targets the streak instabilities closer to the center plane.

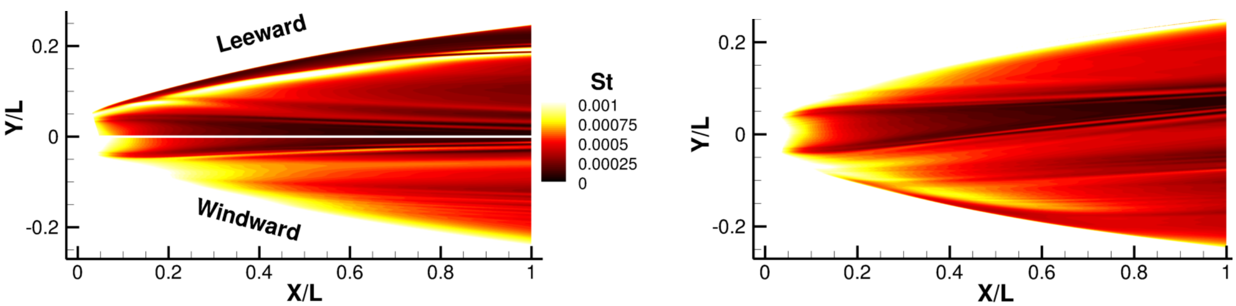

(a) Case FAL$_\alpha$ (Note that the leeward and windward sides are not physically contiguous and have been shown as mirror images of each other purely for convenience of illustration.)

(b) Case FAL$_\beta$: The port side corresponds to the windward side (bottom), whereas the starboard side corresponds to the leeward side on the top.

Fig. 2. Stanton number contours for Cases FAL$_\alpha$ (mesh FAL$_{2Z,b}$) and FAL$_\beta$ (mesh FAL$_{2Y,b}$). [27]

Cross-plane contours of the Mach number distributions at selected axial stations for the FAL$_\alpha$ case are shown in Figs. 3 and 4 for the leeward and windward sides, respectively. These figures indicate a qualitatively different streak evolution on the two sides. The Mach number contours on each side within the aft portion of the model (i.e., X/L > 0.50) indicate two prominent rolled-up structures resembling inclined mushrooms near the transition between the region of thickened boundary layer in the middle to a thinner boundary layer on either side. However, on the windward side, there are significant differences between those two structures. Specifically, Figs. 4(c) and 4(d) indicate that the inboard structure (i.e., the one closer to the center plane at Y/L = 0) rolls up earlier and is appreciably greater in size in comparison with the outboard structure adjacent to it. On the other hand, the Mach number contours on the leeward side indicate that the two structures at each of the aft locations in Figs. 3(c) and 3(d) are very similar in size as well as in the respective roll-up locations. As shown in the following section, these differences in streak structures lead to large differences between the amplification characteristics on the windward and the leeward sides. Although not shown, the angle of attack also modifies the flow behavior in the vicinity of the leading edges, leading to the formation of rollup structures adjacent to the leading edge on the leeward side, and also on the gutter side of the windward leading edge. The instability characteristics of the former structures on the instability of the boundary layer flow over the test surface are examined in Section IV of this paper.

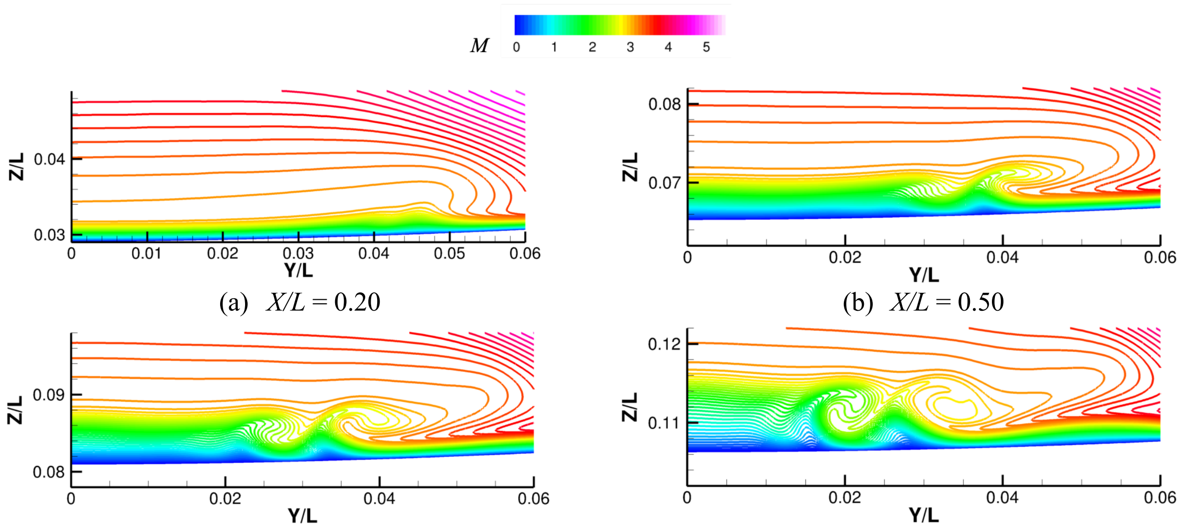

(a) $X/L = 0.20$ (b) $X/L = 0.50$

(c) $X/L = 0.63$ (d) $X/L = 0.84$

Fig. 3. Mach number contours of the basic state near the leeward symmetry plane for Case FAL$_\alpha$ (mesh FAL$_{2Z,b}$). Contour values range from 0 to 5, in increments of 0.1.

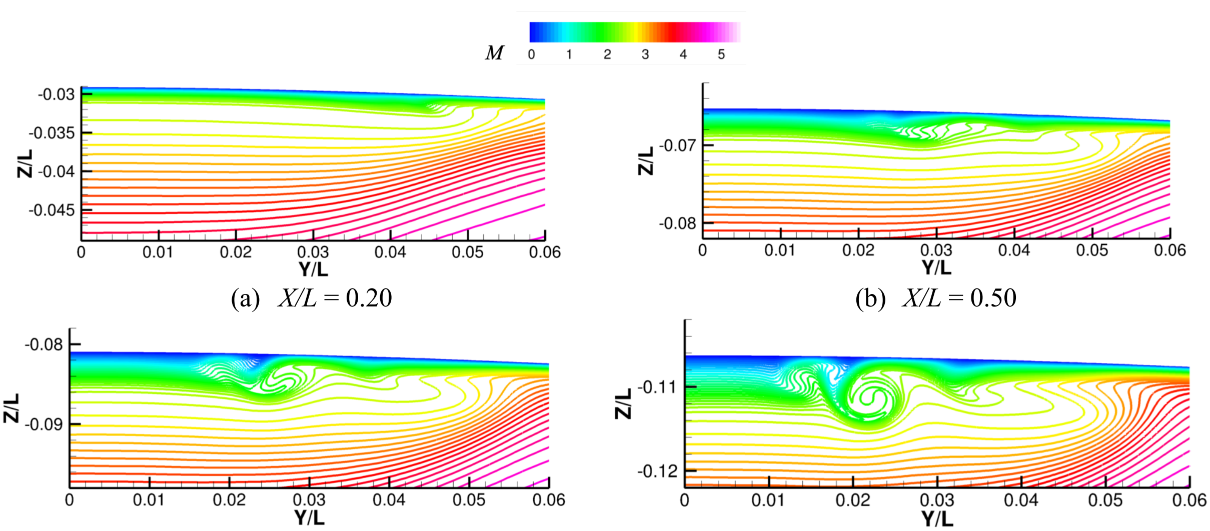

(a) $X/L = 0.20$ (b) $X/L = 0.50$

(c) $X/L = 0.63$ (d) $X/L = 0.84$

Fig. 4. Mach number contours of the basic state near the windward symmetry plane for Case FAL$_\alpha$ (mesh FAL$_{2Z,b}$). Contour values range from 0 to 5, in increments of 0.1.

Mach number contours at the same set of locations for the FAL$_\beta$ case are displayed in Fig. 5. Due to the nonzero angle of yaw, the region of thickened boundary layer behind the 2D nose tip is now shifted to the right, i.e., toward the leeward side. Indeed, at $X/L = 0.63$ and $X/L = 0.84$, both sets of rolled-up structures (i.e., streaks) near the azimuthal boundaries of the central region of thicker boundary layer are now located on the right hand side of the geometric symmetry plane ($Y/L = 0$) of the model. Similar to the previously discussed evolution in the FAL$_\alpha$ case, there is a prominent asymmetry between the rollups of the Mach number contours on either end of the region of thickened boundary layer. In particular, the relative strengths of the rolled-up structures indicate significant variations between the two sides. These variations, in turn, lead to significant differences between the amplification characteristics of the streak instabilities as described in Section IV.

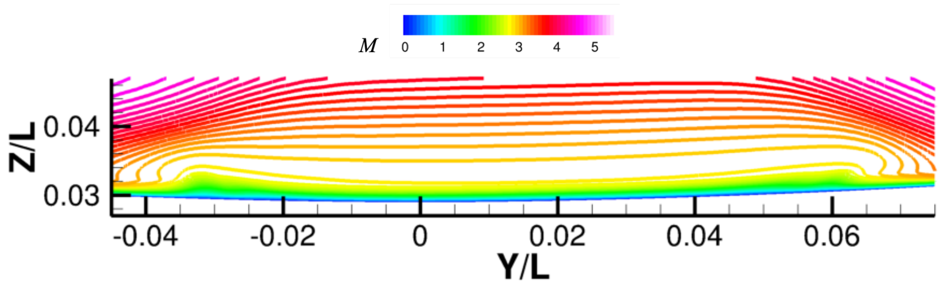

(a) $X/L = 0.20$

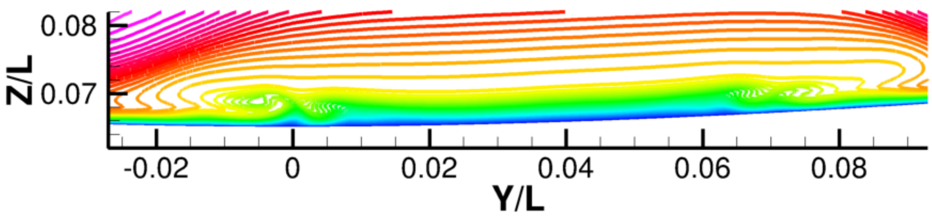

(b) $X/L = 0.50$

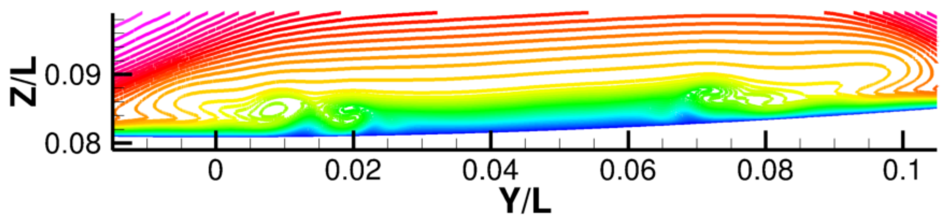

(c) $X/L = 0.63$

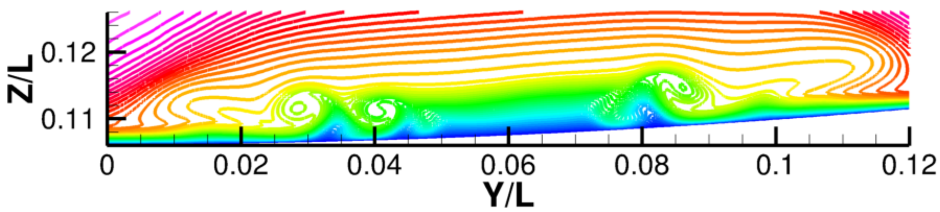

(d) $X/L = 0.84$

Fig. 5. Mach number contours of the basic state near the symmetry plane for Case FAL$_\beta$ (mesh FAL$_{2Y,b}$). Contour values range from 0 to 5, in increments of 0.1.

IV. Streak Instability Characteristics

Computational findings based on the stability analyses of the basic states for the Cases FAL$_\alpha$ and FAL$_\beta$ are outlined in this section. In each case, we begin by presenting the local amplification characteristics and mode structures of the dominant families of unstable modes at selected axial stations. The axial evolution of the overall amplification ratios, i.e., N-factor curves for selected disturbances is presented next, which allows us to infer trends with respect to the effects of a nonzero angle of attack and yaw on the estimated transition locations.

A. Case FAL$_\alpha$

The growth rate spectra for selected families of unstable modes obtained via the partially nonparallel (PNP) eigenvalue analysis [27] of the basic state in the vicinity of the center plane on the leeward side at X/L = 0.515 are shown in Fig. 6(a), along with the mode shapes of the $|u'|$ velocity perturbation for the disturbance frequencies that approximately correspond to the most unstable mode from each family. The white lines in the mode shape plots represent the streamwise velocity contours of the base flow, and the colored contours indicate the magnitude of the axial velocity fluctuations. The associated phase speeds of the modes is plotted in Fig. 6(b). Analogous results for the windward side are shown in Figs. 7(a) and 7(b), respectively.

A total of five different families of unstable modes are plotted in Fig. 6 for the leeward side. For ease of referencing, these mode families are numbered in Fig. 6(a) as I, II, MM (CL), MM (S), and MM (A), respectively, but the ordering of the modes does not have any physical significance. There are additional unstable modes, but they were deemed to be unimportant either because of low overall amplification factors or because their peak fluctuations occur outboard of the prominent streak adjacent to the center plane. For example, disturbances resembling traveling crossflow instabilities can occur in the outboard region, but they are considered to be beyond the scope of the present analysis, which is focused on the region of thick boundary layer near the center plane.

The line contours in white within the mode shape plots of Fig. 6(a) indicate the two rollup structures or the streak regions of interest adjacent to the center plane, specifically, a weaker structure near Y/L = 0.03 and a stronger one near the outboard edge of the thickened boundary layer in the vicinity of Y/L = 0.04. Modes I and II denote the shear layer modes that are concentrated in the regions of high basic state shear within the outer vorticity structure. Mode I, which has the higher amplification rates between these shear layer modes, is concentrated near the top of the outboard streak, whereas Mode II has its peak velocity fluctuations concentrated within the inclined portion of the shear layer along the inboard side of the outer streak. The peak growth rate of Mode I is nearly 50 percent larger than the peak growth rate associated with Mode II. On the other hand, the wall-normal distribution of the velocity fluctuations associated with Mode MM (CL) resembles the typical structure of Mack mode instabilities in the quasi-2D boundary layer in the immediate vicinity of the center line at Y/L = 0. While the wall-normal distribution of Modes MM (S) and MM (A) within the inboard region resembles that of the Mode MM (CL), these two modes also induce a secondary peak in $|u'|$ fluctuations within the inner, i.e., secondary rollup region. Furthermore, consistent with the known behavior of the Mack mode instabilities, the frequency bandwidths of Modes MM (CL), MM (S), and MM (A) are substantially lower than the frequency range of the dominant shear layer Mode (Mode I). On the other hand, each of the Mack-mode like disturbances has a higher peak growth rate than that of the Mode I.

Figure 6(a) also indicates that the peak-growth-rate frequency for the Mack mode disturbances shifts to slightly higher values from Mode MM (CL) to Modes MM (S) and MM (A), as the location of the peak modal fluctuations moves away from the center plane. The small increase in the peak frequency is qualitatively consistent with the slight thinning of the boundary layer adjacent to the center plane as seen from the line contours of the basic state within the mode shape plots. The growth rates as well as the phase speeds of both MM (S) and MM (A) modes are nearly the same throughout the range of unstable frequencies at X/L = 0.515, indicating that the symmetry condition at Y/L = 0 has a minimal influence on either mode. The local behavior of the above three modes is believed to be indicative of the overall characteristics of Mack mode instabilities in boundary layer flows that are weakly inhomogeneous in the azimuthal (or spanwise) direction. In other words, their behavior as captured in Fig. 6 is believed to be generic to the resonances of trapped acoustic modes in predominantly unidirectional boundary layer flows whose thickness (and, hence, the effective channel height for the trapped waves) varies slowly in the azimuthal direction. Thus, a similar modal topology is also expected to be seen within primarily 2D boundary layer flows over other hypersonic configurations. Figure 6(b) shows that the axial phase speeds of the Mack mode families are very close to each other at any given frequency. Among the two shear layer modes (Modes I and II), the phase speeds of Modes I are significantly lower than those of the Mode II disturbances, consistent with the fact that Mode II is concentrated in the inclined shear layer, as against the concentration of the Mode I fluctuations along the crest of the rollup structure.

On the other hand, the growth rate spectra in Fig. 7(a) demonstrate that the peak growth rates of the streak instabilities on the windward side are significantly higher than those of any unstable modes at the same location on the leeward side (Fig. 6(a)). In particular, the peak growth rate for Mode I disturbances on the windward side is more than twice as large as the peak growth rate of any unstable mode near the leeward center plane. Also, all three streak instability modes on the windward side (i.e., Modes I through II) are concentrated within the shear layer near the top of the rollup structure near the outboard edge of the thickened boundary layer. The rapid change in boundary layer thickness at this azimuthal location is associated with the change in entropy layer behavior due to the transition from the 2D nose tip to the highly swept leading edges of the BOLT configuration. We also note that the frequency range of the dominant shear layer mode (Mode I) is very similar on both windward and leeward sides of the model; however, a comparison between Figs. 6(b) and 7(b) also indicates that the phase speed of the Mode I disturbances on the windward side is significantly lower than that on the leeward side.

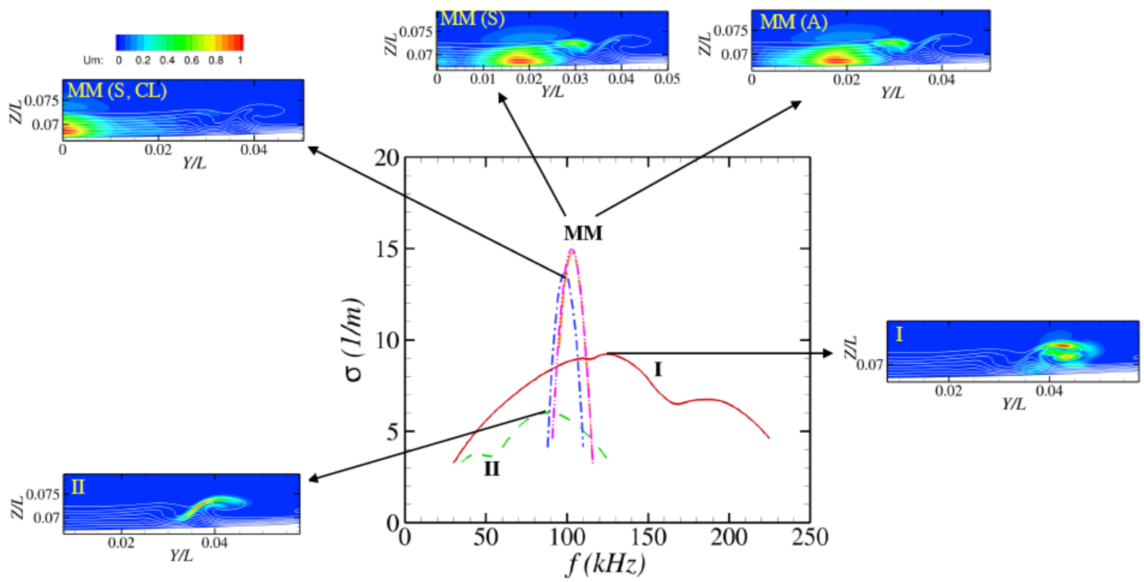

(a) Growth rate spectra and associated mode shapes.

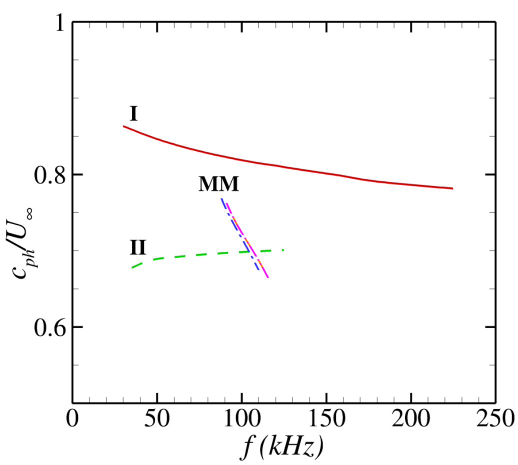

(b) Phase speed spectra (line colors identical to mode families indicated in part (a)).

Fig. 6. Case FAL$_\alpha$: Growth rate and phase speed as functions of frequency for the relevant instability modes on the leeward side at *X/L* = 0.515. The representative mode shapes of each family indicate the |*u*'| fluctuations associated with the locally most unstable disturbance frequency from that family. The |*u*'| values are normalized to a peak value of unity. The growth rate spectra as well as phase velocity curves for the symmetric mode MM (S) and antisymmetric mode MM (A) are nearly identical to each other.

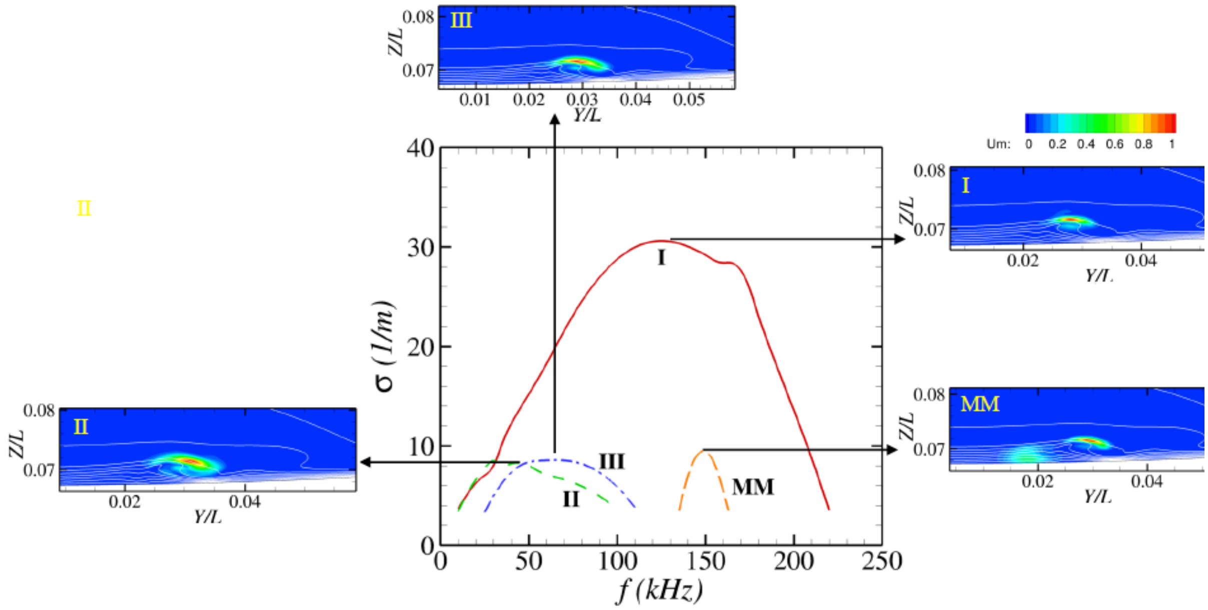

(a) Growth rate spectra and associated mode shapes

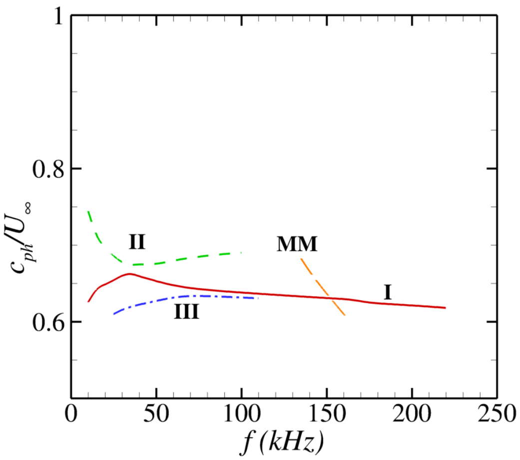

(b) Phase speed spectra (line colors identical to mode families indicated in part (a))

Fig. 7. Case FAL$_\alpha$: Growth rate and phase speed as functions of frequency for the relevant instability modes on the windward side at X/L = 0.515. The representative mode shapes of each family indicate the |u'| fluctuations associated with the locally most unstable disturbance frequency from that family. The |u'| values are normalized to a peak value of unity. To allow for easier visual comparison of the mode shapes with those on the leeward side, the direction of the Z axis is reversed in part (a).

The evolution of PSE based N-factors for constant frequency disturbances from three dominant families of unstable disturbances on the leeward side of the FAL$_\alpha$ case is shown in Fig. 8(a). The highest N-factors based on the amplification of disturbance energy correspond to the disturbance family indicated by blue curves. These disturbances resemble the Mack modes during the early phase of their amplification, and hence, they are denoted as the Mode family MM. The other two groups of instabilities indicated via red and green N-factor curves correspond to shear layer instabilities within the streak region. Accordingly, they are denoted as streak instabilities, abbreviated as SI modes. The streamwise evolution of the most amplified mode of instability from the MM group is shown in Fig. 8(b).

The frequency of this mode is equal to 90 kHz and it achieves the highest N-factor of nearly 6 on the leeward side. At upstream stations, this mode displays multiple azimuthal peaks within the quasi-2D region adjacent to the center plane, suggesting that this mode resembles an oblique Mack mode during the initial phase of its amplification. Fig. 8(b) reveals that, as the streaks within the rollup region become stronger with increasing *X/L*, the peak velocity fluctuations associated with this mode shift to the top of the shear layer associated with the inner rollup region for *X/L* ≥ 0.73.

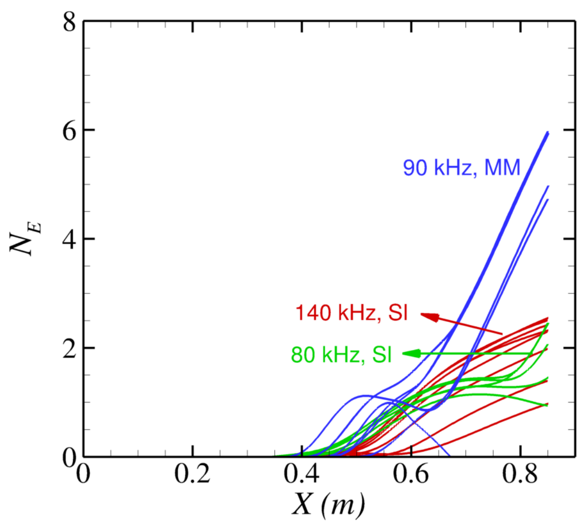

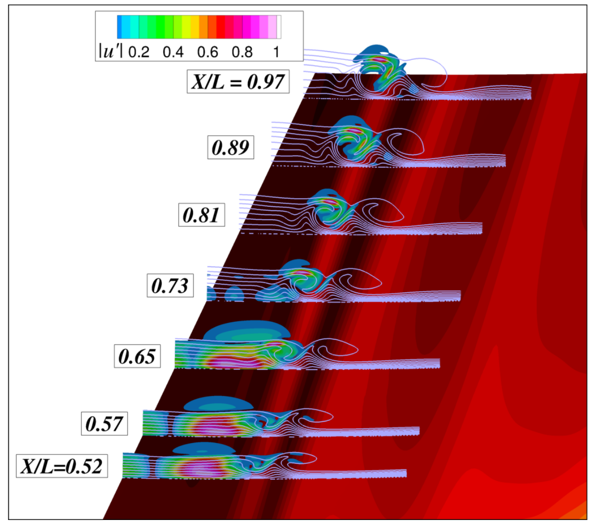

(a) N-factor curves for selected constant-frequency disturbances from dominant families of unstable modes on the leeward side.

(b) $|u'|$ mode-shape evolution for an instability wave with f = 90 kHz from Mode Family MM in part (a).

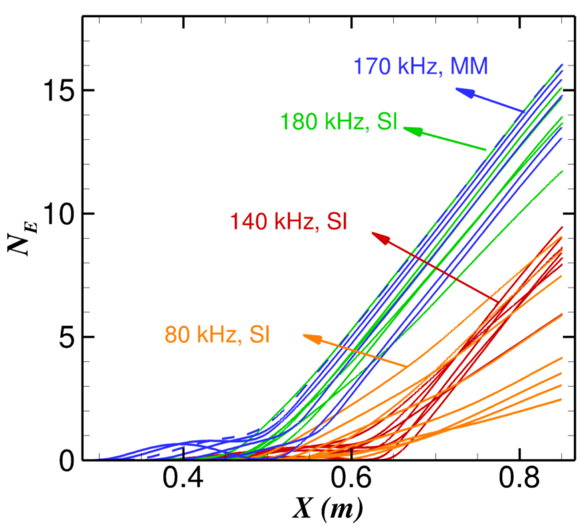

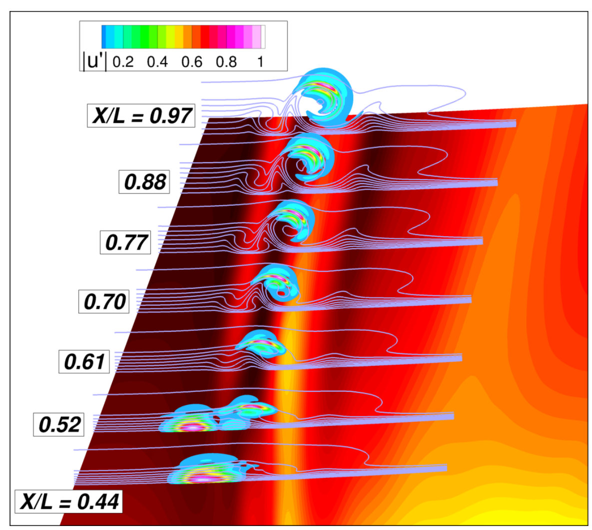

(c) N-factor curves for selected constant-frequency disturbances from dominant families of unstable modes on the windward side.

(d) $|u'|$ mode-shape evolution for an instability wave with f = 170 kHz from Mode Family MM in part (c).

Fig. 8. Amplification characteristics and mode shape evolution predicted by the plane-marching PSE for case FAL$_\alpha$.

Analogous predictions for the windward side are shown in Figs. 8(c) and 8(d), respectively. The set of N-factor curves shown in blue corresponds to the Mode Family MM (i.e., disturbances that originate as Mack modes) , whereas the green and red curves represent purely streak instabilities. The blue curve for the MM disturbance with f = 170 kHz is shown with a dashed line to distinguish it from a closely overlapping curve for the SI Mode at f = 180 kHz. Both the MM family and the dominant family of the SI modes achieve substantially higher N-factors than the peak N-factor on the leeward side. With peak N-factors of 15 and above, the above two families are predicted to dominate the disturbance amplification at this flight condition. The dominant Mode MM disturbance corresponds to a frequency of f = 170 kHz, which achieves a peak N-factor of $N_{max} \approx 16$. The SI Mode at f = 180 kHz also achieves a nearly same N-factor. We note that analogous analysis for a single trajectory point of the HIFiRE-5b flight had suggested that the N-factor at the in-flight transition location was approximately between 14 to 15 [7]. Thus, it seems very likely that the streak instabilities would initiate transition on the windward side at the flight condition of 4-degrees angle of attack, whereas the flow adjacent to the center plane on the leeward side is expected to remain laminar unless and until transition occurs due to contamination from the potentially turbulent regions within the outer regions with a thinner boundary layer.

The mode shape evolution of the dominant Mode MM disturbance at f = 170 kHz is shown in Fig. 8(d), where again the PSE predictions for the $|u'|$ mode shapes at selected streamwise locations are superimposed on the heat flux contours along the surface of the BOLT flight article. The above disturbance originates as a Mack mode just upstream of X/L = 0.44, with a disturbance peak that is close to the model surface and with significant fluctuations across the entire thickness of the boundary layer. As the streak structure becomes stronger in the downstream direction (X/L = 0.52), the shear layer near the edge of the boundary layer also develops relatively strong fluctuations. At the same time, its near-wall signature appears to develop two distinct peaks in the azimuthal direction. Both of these near-wall peaks disappear at the downstream stations and are not observed at any of the locations starting at X/L = 0.61. The above disturbance appears to become purely a mushroom-cap mode in the downstream region.

B. Case FAL$_\beta$

As discussed in Section III, the nonzero yaw angle of β = 4 degrees leads to a prominent azimuthal asymmetry in the boundary layer over the main test surface of the BOLT model. Not only is the region of the thickened boundary layer inclined with respect to the geometric centerplane of the model, but there are also appreciable differences between the rollup of the Mach number contours near the port- and starboard-side boundaries, respectively, of the region of the thicker boundary layer near the middle of the main test surface. Naturally, one would expect these differences to result in commensurately large variations between the stability characteristics on the two sides. Furthermore, as a result of the symmetry breaking due to the yaw angle, the unstable perturbations can no longer be decomposed into symmetric and asymmetric modes as in Section IV.A and, hence, the domain used for the stability analysis must include the entire azimuthal region that is perturbed by the instability modes of interest.

The growth rate spectra for selected families of unstable modes obtained via the partially nonparallel (PNP) eigenvalue analysis of the asymmetric basic state near the center plane are shown in Fig. 9(a) for X/L = 0.343, along with the mode shapes of the $|u'|$ velocity perturbation for the disturbance frequencies that approximately correspond to the most unstable mode from each family. Again, the white lines in the mode shape plots represent the streamwise velocity contours of the base flow, and the colored contours indicate the magnitude of the axial velocity fluctuations. The phase speeds of the various modes from Fig. 9(a) are plotted in Fig. 9(b). Analogous results for X/L = 0.687 are shown in Figs. 10(a) and 10(b), respectively. Even though the instability analysis had revealed additional families of unstable modes at each location, only a selected subset of unstable modes with larger peak growth rates have been plotted in these figures.

The growth rate spectra in Fig. 9(a) are loosely analogous to those found in the wake of an egg-crate roughness pattern within a Mach 5.3 boundary layer [38]. Specifically, the dominant mode families are divided into two separate subclasses. The high-frequency modes correspond to a narrow band of frequencies between 160 kHz and 200 kHz, whereas the lower-frequency modes appear to cover a broader range of frequencies between approximately 0 and 170 kHz. The peak growth rates of these two groups are very close to each other at the streamwise location considered in this figure (X/L = 0.343). The corresponding mode shapes from the same figure also reveal that the high-frequency modes correspond to Mack mode like disturbances, with peak velocity fluctuations concentrated closer to the surface. Mode III (W) is concentrated just inboard of the streak structure on the windward side, whereas mode IV (L) has its peak fluctuations on the inner side (i.e., within the region of quasi-2D, thickened boundary layer) of the leeward side streak. Unlike the baseline case of $\alpha = \beta = 0$ degrees that exhibits an azimuthally symmetric boundary layer flow [27], there is only a single family of Mack-mode like unstable disturbances on both leeward and windward sides for the case of β = 4 degrees. One also observes that the lower-frequency disturbances in Fig. 9(a) are concentrated within the shear layer region near the top of the rollup structure on the windward side. Of the two families within this subgroup of unstable modes, the family II (W) has the higher peak growth rate at this location in comparison with the other family, namely, Mode I (W). The latter family corresponds to a larger bandwidth of frequencies and higher phase speeds than the family II (W) (Fig. 9(b)).

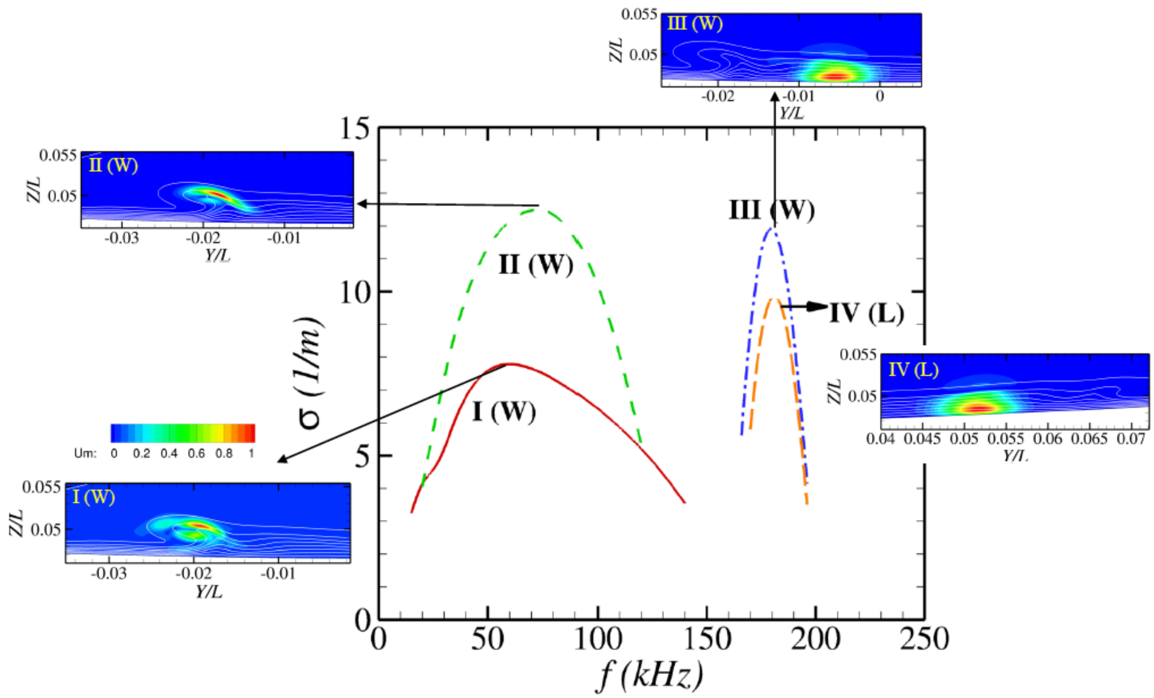

(a) Growth rate spectra and associated mode shapes

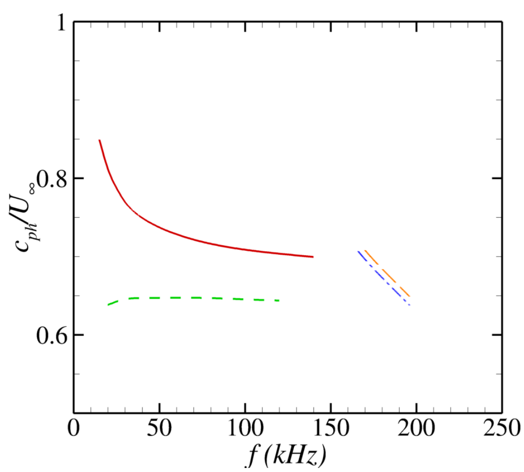

(b) Phase speed spectra (line colors identical to mode families indicated in part (a))

Fig. 9. Case FAL$_\beta$: Growth rate and phase speed as functions of frequency for the relevant instability modes at *X/L* = 0.343. The label within the parentheses next to the mode number indicates whether the mode is concentrated on the windward (W) or the leeward (L) side. The representative mode shapes of each family indicate the |*u*'| fluctuations associated with the locally most unstable disturbance frequency from that family. The |*u*'| values are normalized to a peak value of unity.

As the streak rollup becomes stronger at farther downstream stations, the spectrum of unstable modes becomes richer, with an increased number of unstable modes, a higher frequency bandwidth, and larger peak growth rates. At *X/L* = 0.458 (not shown in this paper), one still finds a similar pair of Mack modes at nearly the same frequencies; however, the streak instabilities now extend in frequency up to nearly 500 kHz and the peak growth rate of the latter family of disturbances is more than three times as large as the peak growth rate at X/L = 0.343. Figure 10(a) shows that at the even farther downstream station of X/L = 0.687, one can no longer observe any Mack-mode like disturbances, and all dominant instability modes now correspond to streak instabilities alone. The basic state on the windward side at this station includes two dominant rollup structures and one finds multiple unstable modes that are concentrated in the shear layer at the top of either one of these structures.

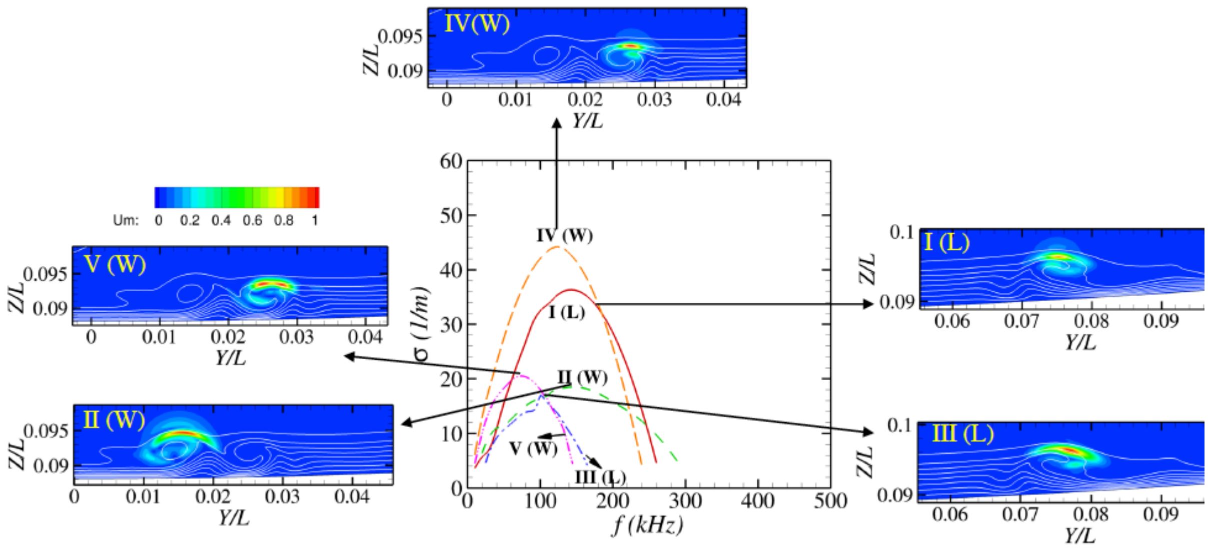

(a) Growth rate spectra and associated mode shapes

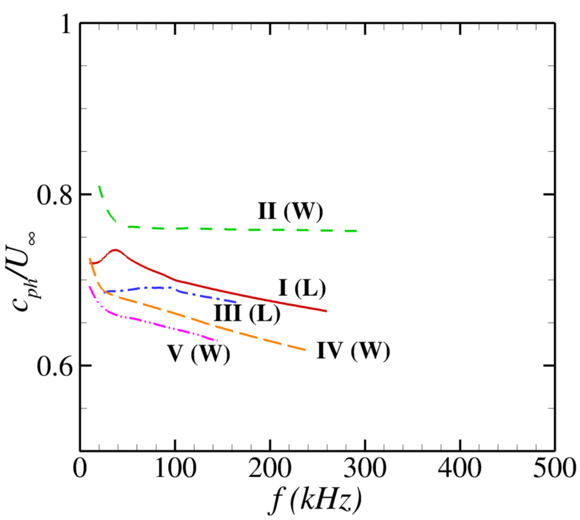

(b) Phase speed spectra (line colors identical to mode families indicated in part (a))

Fig. 10. Case FAL$_\beta$: Growth rate and phase speed as functions of frequency for the relevant instability modes at X/L = 0.687. The label within the parentheses next to the mode number indicates whether the mode is concentrated on the windward (W) or the leeward (L) side. The representative mode shapes of each family indicate the $|u'|$ fluctuations associated with the locally most unstable disturbance frequency from that family. The $|u'|$ values are normalized to a peak value of unity.

Figure 10(a) further indicates that the streak instability modes within the inner streak have the highest growth rates, with the peak local growth rate at X/L = 0.687 being nearly three times larger than the maximum growth rate at the upstream station of X/L = 0.343 (Fig. 9(a)). Because the instability modes within the inner streak (Modes IV (W) and

V (W)) are located further below the edge of the boundary layer in comparison to the instability mode in the outer streak (Mode II (W)) on the windward side, the phase speeds of the former two modes are also lower than those of the unstable modes within the outer streak (Fig. 10(b)). The leeward side shows a single streak and, therefore, both of the dominant instability modes on the leeward side (i.e., Modes I (L) and III (L)) are concentrated within that streak.

The evolution of PSE based N-factors for the selected dominant families of unstable modes on the leeward side is shown in Fig. 11(a). The blue set of curves correspond to modes that originate as Mack modes and morph into streak instabilities in the downstream region (approximately for $X > 0.55$ m). Both the growth rates and the extent of cumulative amplification during the streak instability phase is substantially larger than that during the earlier phase as Mack modes. The overall amplification as Mack mode disturbances is rather modest, equal to an N-factor of approximately one or less. The green curves in Fig. 11(a) represents the disturbances that correspond to streak instabilities throughout their region of amplification. These modes become unstable farther downstream ($X > 0.50$ m, or equivalently, $X/L > 0.58$) in comparison with the Mack-mode like disturbances. However, both the frequencies and the growth rates of those modes are similar to those of the Mack modes after they have morphed into streak instabilities.

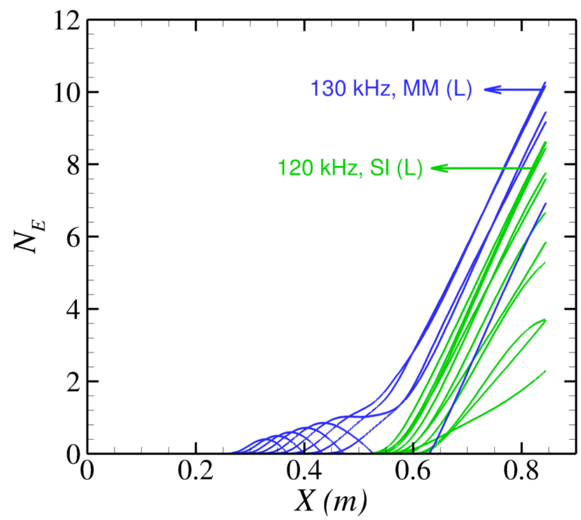

(a) N-factor curves for selected constant-frequency disturbances from dominant families of unstable modes

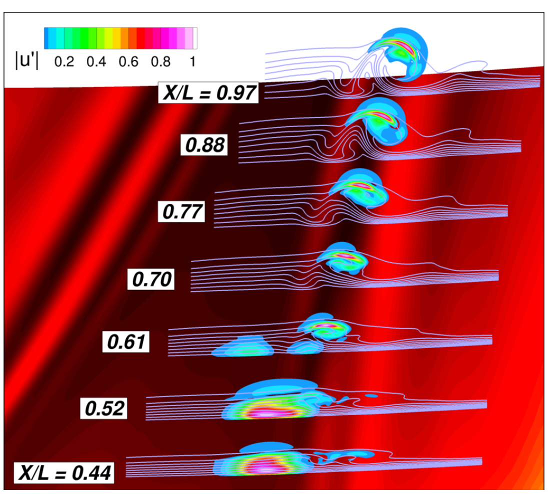

(b) $|u'|$ mode-shape evolution for Mack-mode disturbance with $f = 130$ kHz

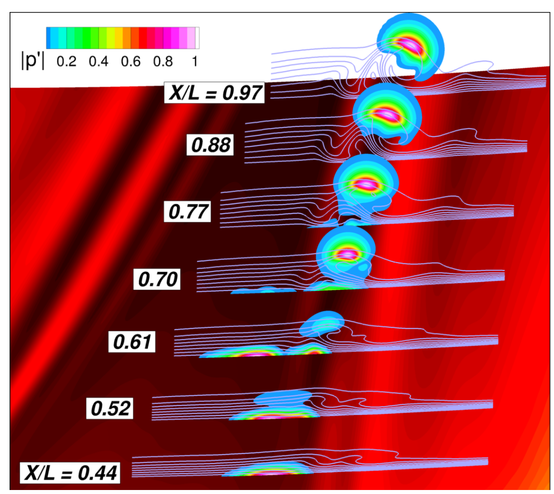

(c) $|p'|$ mode-shape evolution for Mack-mode disturbance with $f = 130$ kHz

Fig. 11. Amplification characteristics and mode shape evolution predicted by the plane marching PSE for case FAL$_\beta$ (leeward side).

Because of their extra initial amplification as Mack modes, the latter group of disturbances (blue curves) are able to achieve somewhat higher N-factors than the purely streak instabilities (green curves) and, therefore, are likely to dominate the disturbance amplification at this flight condition. The modes denoted via blue curves may also be referred to as the hybrid modes because of their dual character as Mack modes upstream and streak instability downstream. The dominance of the hybrid instability modes is rather analogous to the computations of high-frequency secondary instabilities in three-dimensional hypersonic boundary layers with finite amplitude stationary crossflow vortices [39, 40].

The dominant hybrid disturbance in Fig. 11(a) corresponds to a frequency of $f = 130$ kHz, which attains a peak N-factor of $N_{max} \approx 10$, i.e., slightly smaller than the peak N-factor of around 11 at the design condition of $\alpha = \beta = 0$ deg. The mode-shape evolution of the $|u'|$ fluctuations associated with the above disturbance is shown in Fig 11(b). At the two farthest upstream stations, i.e., for $X/L = 0.44$ and $X/L = 0.52$, the highest velocity fluctuations occur on the inner side of the rollup region (i.e., toward the side of the boundary-layer thickening), consistent with the Mack mode behavior during the early phase of amplification. However, at $X/L = 0.61$, the peak fluctuations have shifted to the shear layer that bounds the rollup structure on the leeward side from above. Indeed, for $X/L \geq 0.70$, there is hardly any trace of the near-wall peak and this unstable mode appears to have become a purely streak instability. The corresponding evolution of the $|p'|$ mode shapes in Fig. 11(c) also highlights the progressive weakening of the surface pressure fluctuations as the disturbance transitions from a Mack mode to a streak instability and then continues to lift up further away from the surface. The associated change in the mode shape of the $|p'|$ fluctuations counteracts the exponential increase in the surface $|p'|$ values and, therefore, the peak N-factor values for the hybrid disturbances are significantly lower than their N-factors based on the disturbance energy as shown in Fig. 11(a). Whereas the peak value of N_E for the hybrid disturbances is close to 10, the corresponding maximum of the N-factor based on the maximum wall pressure fluctuation is slightly less than 6, which is also slightly less than the wall-pressure based N-factor for the purely streak instabilities. In other words, surface pressure measurements of the hybrid instability modes that originate as Mack modes are likely to significantly underestimate the amplification of the velocity fluctuations.

The predicted disturbance evolution on the windward side as shown in Figs. 12(a) and 12(b) is quite similar to that on the leeward side from Fig. 11. The windward side does support an additional family of purely streak instabilities associated with the outermost rollup structure (see Mode II (W) in Fig. 10(a)) as indicated by the group of red curves. However, the overall amplification potential of this family is lower than the other two families that are indicated by the blue curves (hybrid Mack mode disturbances) and the green curves (streak instabilities), respectively.

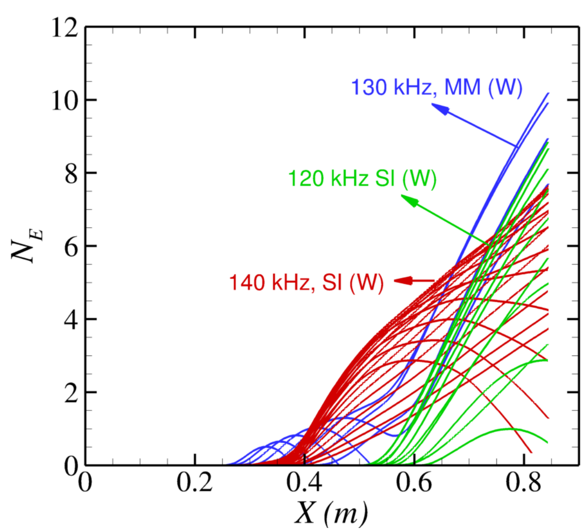

(a) N-factor curves for selected constant-frequency disturbances from dominant families of unstable modes

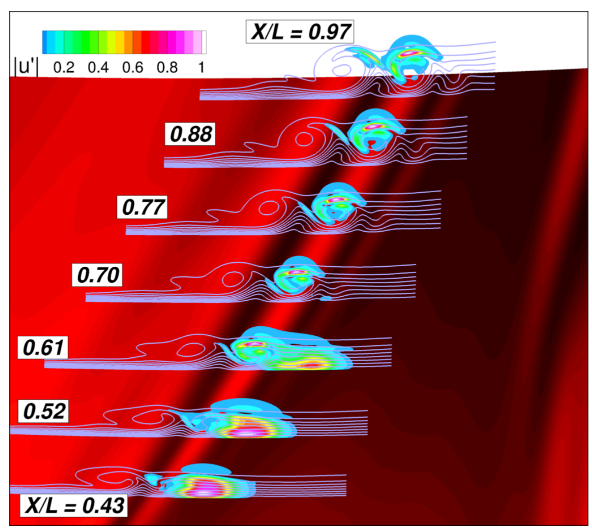

(b) Mode shape evolution for Mode Family 1 with $f = 130$ kHz

Fig. 12. Amplification characteristics and mode shape evolution predicted by the plane marching PSE for case FAL$_\beta$ (windward side).

The highest value of N_E on the windward side corresponds to a hybrid disturbance with $f = 130$ kHz, and the N-factor evolution of this mode is very similar to the most amplified disturbance on the leeward side. In other words, despite the prominent asymmetry of the basic state, the peak N-factors on both leeward and windward sides are very close to each other and, moreover, are somewhat smaller than those at the design condition of $\alpha = \beta = 0$ deg. As previously mentioned, an earlier analysis of streak instabilities for a single trajectory point of the HIFiRE-5b flight had suggested that the N-factor at the measured transition location was in the range of 14 to 15 [13]. Thus, the results in Figs. 11 and 12 suggest that the streak instabilities have a low likelihood of initiating transition at the present yaw angle.

V. Summary and Concluding Remarks

This paper represents the continuation of the previous numerical studies pertaining to the streak instabilities within the region of boundary layer thickening near the center plane of nonaxisymmetric hypersonic configurations. Specifically, the analysis of streak instabilities adjacent to the center plane of the BOLT flight configuration is extended to include the effects of a nonzero angle of attack and a nonzero yaw angle at a selected point from the ascent portion of the anticipated flight trajectory ($t = 28.8767$ sec, $M_\infty = 5.53$, and $Re_L = 4.25\times10^6$). Either type of attitude modification is shown to have a prominent effect on the overall streak pattern over the model, including the streaks on either side of the region of boundary layer thickening near the middle of the main test surface.

A nonzero yaw of $\beta = 4$ deg (at $\alpha = 0$ deg) is shown to produce a strongly asymmetric streak pattern between the port- (i.e., windward) and starboard-side (leeward) boundaries, respectively, between the azimuthal regions of thicker and thinner boundary layers. However, despite the large change in the streak evolution, the character of the dominant instabilities and the peak N-factors are nearly the same between the windward and the leeward sides. Furthermore, the peak N-factor values on both sides of the yawed configuration are only slight smaller than those found in the earlier study for the design condition of $\alpha = \beta = 0$ deg.

On both sides of the region of the thickened boundary layer, the highest N-factors based on the disturbance energy correspond to hybrid modes that begin to amplify as Mack modes and subsequently morph into primarily streak instabilities when the stationary rollup structures become increasingly stronger along the downstream direction. These hybrid modes have a strong pressure signature at the surface during the early phase of their amplification. However, as they migrate away from the surface to become concentrated within the shear layer near the top of the streak, the pressure signature becomes very weak. Consequently, even as the peak velocity fluctuations amplify rapidly, the surface pressure fluctuations fail to keep pace, and hence, any surface-based pressure sensors would predict significantly lower amplification factors for these modes, in comparison with the amplification of the velocity fluctuations.

In contrast to the relatively small effects of $\beta = 4$ deg on the overall amplification of instabilities near the middle of the test surface, an angle of attack of $\alpha = 4$ deg is found to have a relatively profound effect on the magnitude of the instability amplification. Specifically, the peak N-factor on the windward side at $\alpha = 4$ deg (and $\beta = 0$ deg) is approximately 16, in comparison to the substantially lower value of nearly 6 on the leeward side. In contrast, the peak N-factor at the design condition of $\alpha = \beta = 0$ deg was equal to nearly 11, i.e., nearly the same as the arithmetic mean of the peak N-factor values on the windward and leeward sides, respectively, in the $\alpha = 4$ deg case. The N-factor value of 11 at the design condition is lower than the N-factor of 14 that correlated with Mack-mode transition on the HIFiRE-1 flight configuration, but close to the N-factor range where transition onset has been observed in subsonic and supersonic flows, it is difficult to predict whether or not the streak instabilities on either side of the centerline would initiate transition $\alpha = \beta = 0$ deg. On the other hand, one may assert with a greater degree of confidence that transition would not occur on the leeward side when $\alpha = 4$ deg (because the peak N-factor is much lower), and that transition would be very likely to happen on the windward side at the flow conditions investigated herein (due to the significantly higher peak N-factor). Of course, we emphasize that the computational findings reported herein are limited to the streaks on either side of the region of the thickened boundary layer. Our related ongoing work is focused on the effects of the angle of attack and the yaw on the instability evolution within other parts of the test surface, including localized azimuthal regions within the region of a thinner boundary layer wherein strong streaks may occur and possibly dominate transition under certain flow conditions. Furthermore, similar computations for the descent phase of the flight trajectory will be undertaken in the future.

Acknowledgments

This work was supported by the Hypersonic Technology Project. Computational resources for this research were provided by the NASA High-End Computing (HEC) Program through the NASA Advanced Supercomputing (NAS)

Division at Ames Research Center. The authors express their gratitude to Mr. Jeffery White and Dr. Robert Baurle for their advice concerning the VULCAN computations described in this paper.

References

1. Dougherty, N. S. and Fisher, D. F., "Boundary Layer Transition on a 10-degree Cone:Wind Tunnel/Flight Data Correlation," AIAA Paper 1980-0154, 1980.
2. Sherman, M. M., and Nakamura, T., "Flight Test Measurements of Boundary-Layer Transition on a Nonablating 22-Degree Cone," *Journal of Spacecraft and Rockets*, Vol. 7, No. 2, 1970, pp. 137–142.
3. Carter, H. S., Raper, J. L., Hinson, W. F., and Morris, W. D., "Basic Measurements from a Turbulent-Heating Flight Experiment on a 5° Half-Angle Cone at Mach 20 (Reentry F)," NASA TM X-2308, 1971.
4. Johnson, C. B., Stainback, P. C., Wicker, K. C., and Bony, L. R., "Boundary-Layer Edge Conditions and Transition Reynolds Number Data for a Flight Test at Mach 20 (Reentry F)," NASA TM X-2584, 1972.
5. Malik, M. R., Li, F., and Choudhari, M., "Analysis of Crossflow Transition Flight Experiment aboard the Pegasus Launch Vehicle," AIAA Paper 2007-4487, 2007.
6. Berry, S., Daryabeigi, K., Wurster, K., and Bittner, R., "Boundary-Layer Transition on X-43A," *Journal of Spacecraft and Rockets*, Vol. 47, No. 6, 2010, pp. 922–934. https://doi.org/10.2514/1.45889
7. Kimmel, R. L., Adamczak, D., Paull, A., Paull, R., Shannon, J., Pietsch, R., Frost, M., and Alesi, H., "HIFiRE-1 Ascent-Phase Boundary-Layer Transition," *Journal of Spacecraft and Rockets*, Vol. 52, No. 1, 2015, pp 217-230. https://doi.org/10.2514/1.A32851
8. Li, F., Choudhari, M., Chang, C.-L., Kimmel, R., Adamczak, D., and Smith, M., "Transition Analysis for the Ascent Phase of HIFiRE-1 Flight Experiment," *Journal of Spacecraft and Rockets*, Vol. 52, No. 5, 2015, pp. 1283-1293. https://doi.org/10.2514/1.A33258
9. Kimmel, R. L., Adamczak, D. A., and DSTG AVD Brisbane Team, "HIFiRE-5b Flight Overview," AIAA Paper 2017-3131, June 2017. https://doi.org/10.2514/6.2017-3131
10. Tufts, M. P., Gosse, R., and Kimmel, R. L., "PSE Analysis of Crossflow Instability on HIFiRE 5b Flight Test," AIAA Paper 2017-0764, January 2017. https://doi.org/10.2514/6.20178-0764
11. Choudhari, M., Chang, C.-L., Li, F., Berger, K., Candler, G., and Kimmel, R., "Transition Analysis for the HIFiRE-5 Vehicle," AIAA Paper 2009-4056, 2009. https://doi.org/10.2514/6.2009-4056
12. Paredes, P., Gosse, R., Theofilis, V., and Kimmel, R. L., "Linear Modal Instabilities of Hypersonic Flow over an Elliptic Cone," *J. Fluid Mechanics*, Vol. 804, 2016, pp. 442–466. https://doi.org/10.1017/jfm.2016.536
13. Choudhari, M., Li, F., and Paredes, P., "Streak Instabilities on HIFiRE-5 Elliptic Cone," AIAA Paper 2020-0828, 2020. https://doi.org/10.2514/6.2020-0828
14. Wheaton, B., Berridge, C., Wolf, T., Stevens, R., and McGrath, B., "Boundary Layer Transition (BOLT) Flight Experiment Overview," AIAA Paper 2018-2892, 2018. https://doi.org/10.2514/6.2018-2892
15. Wheaton, B., Berridge, C., Wolf, T., Stevens, R., Araya, D., Stevens R., McGrath B., and Adamczak, D., Final Design of the Boundary Layer Transition (BOLT) Flight Experiment," AIAA Paper 2020-1041, 2020. https://doi/abs/10.2514/6.2020-1041
16. Berridge, D. C., McKiernan, G. R., Wheaton, B. M., Wolf, T. D. and Schneider, S. P., "Hypersonic Ground Tests In Support of the Boundary Layer Transition (BOLT) Flight Experiment," AIAA Paper 2018-2893, 2018. https://doi.org/10.2514/6.2018-2893
17. Kostak, H. E., Bowersox, R. D. W., McKiernan, G., Thome, J., Candler, G., and King, R. A., "Freestream Disturbance Effects on Boundary Layer Instability and Transition on the AFOSR BOLT Geometry," AIAA Paper 2019-0088, 2019. https://doi.org/10.2514/6.2019-0088
18. Kostak, H. E. and Bowersox, R. D. W., "Hypersonic Boundary Layer Off-Body and Surface Measurements on the AFOSR BOLT Geometry," AIAA Paper 2020-1043, 2020. https://doi/abs/10.2514/6.2020-1043
19. Berridge, D., Kostak, H., McKiernan, G., King, R., Wason, M., Wheaton, B., Wolf, T., and Schneider, S., "Hypersonic Ground Tests with High-frequency Instrumentation in Support of the Boundary Layer Transition (BOLT) Flight Experiment," AIAA Paper 2019-0090, 2019. https://doi.org/10.2514/6.2019-0090
20. Berry, S. A., Mason, M. L., Greene, F. A., King, R. A., Rieken, E. F., and Basore, K. D., "LaRC Aerothermodynamic Ground Tests in Support of BOLT Flight Experiment," AIAA Paper 2019-0091, 2019. https://doi.org/10.2514/6.2019-0091
21. Thome, J., Dwivedi, A., Nichols, J., and Candler, G., "Direct Numerical Simulation of BOLT Hypersonic Flight Vehicle," AIAA Paper 2018-2894, 2018. https://doi.org/10.2514/6.2018-2894
22. Knutson, A., Thome, J., and Candler, G., "Numerical Simulation of Instabilities in the Boundary-Layer Transition Experiment Flowfield," *Journal of Spacecraft and Rockets*, 2019. https://doi.org/10.2514/1.A34599
23. Thome, J., Knutson, A., and Candler, G., "Boundary Layer Instabilities on BOLT Subscale Geometry," AIAA Paper 2019-0092, 2019. https://doi.org/10.2514/6.2019-0092
24. Thome, J., Reinert, J. D. and Candler, G., "Effect of Steady Forcing on BOLT Flowfield for Flight Reynolds Numbers," AIAA Paper 2020-1042, 2020. https://doi/abs/10.2514/6.2020-1042
25. Moyes, A. J., Kocian, T. S., Mullen, C. D., and Reed, H. L., "Preflight Boundary-Layer Stability Analysis of BOLT Geometry," AIAA 2018-2895, 2018. https://doi.org/10.2514/6.2018-2895

26. Moyes, A. J. and Reed, H. L., "Nonlinear Boundary-Layer Stability Analysis of BOLT and HIFiRE-5," AIAA 2019-2972, 2019. https://doi.org/10.2514/6.2019-2972
27. Li, F., Choudhari, M., and Paredes, P., "Streak Instability Analysis for BOLT Configuration," AIAA Paper 2020-3028, 2020. https://doi.org/10.2514/6.2020-3028
28. http://vulcan-cfd.larc.nasa.gov/index.html (November 17, 2020)
29. van Albada, G. D., van Leer, B. and Roberts, W. W., "A Comparative Study of Computational Methods in Cosmic Gas Dynamics," *Astronomy and Astrophysics*, Vol. 108, pp. 76-84, 1982. https://doi.org/10.1007/978-3-642-60543-7_6
30. Edwards, J. R., "A Low-Diffusion Flux-Splitting Scheme for Navier-Stokes Calculations," *Computer and Fluids*, Vol. 6, pp. 635-659, 1997. https://doi.org/10.1016/S0045-7930(97)00014-5
31. Litton, D., Edwards, J., and White, J., "Algorithmic Enhancements to the VULCAN Navier-Stokes Solver," AIAA Paper 2003-3979, 2003. https://doi.org/10.1017/S0022112010005094
32. Wu, M. and Martin, M. P., "Direct Numerical Simulation of Supersonic Boundary Layer over a Compression Ramp," *AIAA Journal*, Vol. 45, No. 4, 2007, pp. 879-889. https://doi.org/10.2514/1.27021
33. Jiang, G. S. and Shu, C. W., "Efficient Implementation of Weighted ENO Schemes," *J. Comp. Phys.*, Vol. 126, No. 1, 1996, pp. 202-228. https://doi.org/10.1006/jcph.1996.0130
34. Taylor, E. M., Wu, M., and Martin, M. P., "Optimization of Nonlinear Error Sources for Weighted Non-Oscillatory Methods in Direct Numerical Simulations of Compressible Turbulence," *J. Comp. Phys.*, Vol. 223, No. 1, 2006, pp. 384-397. https://10.1016/j.jcp.2006.09.010
35. Williamson, J., "Low-Storage Runge-Kutta Schemes," *J. Comp. Phys.*, Vol. 35, No. 1, 1980, pp. 48-56. https://doi.org/10.1016/0021-9991(80)90033-9
36. Paredes, P., Hanifi, A., Theofilis, V., and Henningson, D., "The Nonlinear PSE-3D Concept for Transition Prediction in Flows with a Single Slowly-Varying Spatial Direction," Procedia IUTAM, Vol. 14C, 2015, pp. 35-44.
37. Mullen, D. and Reed, H. L., "Linear Parabolized Stability Analysis of the BOLT Flight Geometry at Off-Nominal Conditions," AIAA Paper 2020-3027, 2020. https://doi.org/10.2514/6.2020-3027
38. Choudhari, M., Li, F., and Paredes, P., "Effect of Distributed Patch of Smooth Roughness Elements on Transition in a High-Speed Boundary Layer," AIAA Paper 2018-3532, 2018. https://doi.org/10.2514/6.2018-3532
39. Li, F., Choudhari, M., Paredes, P., and Duan, L., "High-Frequency Instabilities of Stationary Crossflow Vortices in a Hypersonic Boundary Layer," *Phys. Rev. Fluids*, Vol. 1, 2016, 053603.
40. Choudhari, M., Li, F., Paredes, P., and Duan, L., "Nonlinear Evolution and Breakdown of Azimuthally Compact Crossflow Vortex Pattern over a Yawed Cone," AIAA Paper 2018-1823, 2018. https://doi.org/10.2514/6.2018-1832